Experimental investigation of phase separation in binary dusty plasmas under microgravity

Stefan Schütt,* Michael Himpel, and André Melzer
Institute of Physics, University of Greifswald, 17489 Greifswald, Germany

(Received 14 February 2020; accepted 7 April 2020; published 29 April 2020)

Three-dimensionally extended dusty plasmas containing mixtures of two particle species of different size have been investigated under microgravity conditions. To distinguish the species even at small size disparities, one of the species is marked with a fluorescent dye, and a modified two-camera video microscopy setup is used for position determination and tracking. Phase separation is found even when the size disparity is below 5%. Particles are tracked to obtain the diffusion flux, and resulting diffusion coefficients are calculated to be about -10^{-6} mm^2/s, which is in the expected range for a phase separation process driven by plasma forces. Additionally, a measure for the strength of the phase separation is presented that allows us to quickly characterize measurements. There is a clear correlation between size disparity and phase separation strength.

DOI: 10.1103/PhysRevE.101.043213

I. INTRODUCTION

Phase separation is an interesting topic as it can be studied in a number of widely different systems. There have been studies of phase separation, e.g., in binary liquids [1,2], colloidal systems [3–5], metallic alloys [6,7], and polymer blends [8] as well as dusty plasmas [9–11]. Binary systems, i.e., systems in which mixtures of two particle species are present, belong to the simplest possible class in which phase separation can be studied. They are therefore often chosen for laboratory investigations.

Phase separation in charged particle systems is found due to spinodal decomposition [12] when the charge disparity $\Delta Z/\bar{Z}$ exceeds a certain threshold. In dusty plasmas (according to orbital-motion-limited theory) the charge is proportional to the particle size, so that a large size disparity causes a large charge disparity. In early studies of phase separation in binary dusty plasmas [13,14], the relative size disparity $\varepsilon = \Delta d/\bar{d}$ (where Δd is the difference of the respective diameters of the two particle species and $\bar{d}$ is the mean diameter) has been chosen to be relatively large, i.e., $\varepsilon > 0.2$. In the case of such a large size disparity, the phase separation has been attributed to asymmetries in the interparticle interaction [15].

However, Killer *et al.* have observed that phase separation occurs in binary dusty plasmas even if the size disparity is small ($\varepsilon < 0.05$) [16], which cannot be explained by classical models of spinodal decomposition. It has been found, however, that the phase separation is of a diffusive character, i.e., the particle flux $\vec{J}$ is proportional to the gradient of the particle number density $\vec{\nabla} n$ according to Fick's first law

$$\vec{J} = -D\vec{\nabla} n. \tag{1}$$

Here the proportionality factor D is the diffusion coefficient. Note that D takes negative values in the case of phase separation (*demixing* or *uphill diffusion*), i.e., $\vec{J}$ and $\vec{\nabla} n$ pointing in the same direction. To determine D using this relation, one would need access to the particle number density as well as the particle flux. As their data quality was not good enough to obtain $\vec{J}$ using particle image velocimetry or particle-tracking velocimetry, a different method has been used by Killer *et al.* [16]. The dust cloud was divided into relatively large regions, and $\vec{J}$ was calculated at the region boundaries. The phase separation for this small size disparity has finally been attributed to an imbalance of the plasma forces acting on the particles, namely, the ion drag force and the electric field force. However, the study contained only a very limited set of ε. It is therefore desirable to study binary systems at small size disparities more systematically. Furthermore, better cameras with a higher spatial as well as temporal resolution now allow one to determine the flux $\vec{J}$ with much higher spatial resolution.

When the size disparity is small, two particle species cannot be distinguished based on their scattering intensities. Therefore, a technique using fluorescent particles has been introduced by Killer *et al.* [16]. Particles marked with rhodamine B have been used for one of the species, emitting fluorescence light at a different wavelength than the illumination. Two cameras equipped with appropriate filters have then been used to distinguish the species. Here we present an improved version of that diagnostic setup with two high-resolution video cameras observing the same field of view giving access to the full phase-space information of both particle populations on the single-particle level. The dynamics of the phase separation process has been observed and diffusion coefficients have been obtained from the data. Afterwards, a measure for the strength of the phase separation is introduced that allows us to quickly characterize measurements, making it possible to systematically study phase separation at different plasma parameters and size disparities.

II. EXPERIMENTAL SETUP

The measurements were conducted under microgravity conditions on parabolic flights to generate a three-dimensionally extended dust cloud in which phase separation

*stefan.schuett@physik.uni-greifswald.de

TABLE I. Properties of the used particle mixtures. The mean particle sizes d and standard deviations σ_d are the values given by the manufacturer for the respective batches used. MF denotes pure melamine formaldehyde particles, whereas RhB denotes rhodamine B-dyed particles. See text for the definition of the relative size disparity ε.

No.	d_{MF} (μm)	d_{RhB} (μm)	ε
1	3.50 ± 0.07	3.87 ± 0.08	$+0.100 \pm 0.030$
2	3.55 ± 0.08	4.02 ± 0.09	$+0.124 \pm 0.033$
3	3.81 ± 0.09	3.87 ± 0.08	$+0.016 \pm 0.032$
4	3.81 ± 0.09	4.02 ± 0.09	$+0.054 \pm 0.033$
5	3.93 ± 0.07	3.87 ± 0.08	-0.015 ± 0.028
6	4.04 ± 0.08	3.87 ± 0.08	-0.043 ± 0.029
7	6.50 ± 0.08	6.80 ± 0.17	$+0.045 \pm 0.029$
8	6.78 ± 0.12	7.02 ± 0.08	$+0.035 \pm 0.021$
9	6.84 ± 0.07	7.12 ± 0.15	$+0.040 \pm 0.024$
10	7.01 ± 0.08	6.38 ± 0.15	-0.094 ± 0.025
11	7.01 ± 0.08	7.12 ± 0.15	$+0.016 \pm 0.025$
12	7.01 ± 0.08	7.47 ± 0.12	$+0.064 \pm 0.021$
13	7.17 ± 0.08	6.80 ± 0.17	-0.053 ± 0.027
14	7.17 ± 0.08	7.02 ± 0.08	-0.021 ± 0.016
15	7.23 ± 0.09	7.02 ± 0.08	-0.029 ± 0.017
16	7.30 ± 0.10	7.02 ± 0.08	-0.039 ± 0.018

can be studied. The experiments have been performed in the modified IMPF-K2 plasma chamber described earlier [17]. Here a capacitively coupled radio frequency discharge at 13.56 MHz is ignited between two disk electrodes with a discharge gap of 30 mm and a diameter of 80 mm. The rf power is $P_{\mathrm{rf}} = 1.2$ to 4 W. The working gas is argon at a pressure of $p = 20$ to 40 Pa. Most of the measurements are conducted at $P_{\mathrm{rf}} = 3$ W and $p = 30$ Pa. Dust particles are injected using electromagnetically driven dust shakers. We use monodisperse, spherical melamine formaldehyde particles. Before each flight, the containers of the dust shakers are prepared with mixtures of two types of particles having slightly different mean diameters: one of the species is made of standard melamine-formaldehyde (MF) particles (denoted as MF particles), the other species is made of rhodamine B-doped MF particles (denoted as RhB particles).

A central slice of the particle cloud is illuminated by a vertically expanded green laser sheet with a thickness of about 0.5 mm at a wavelength of $\lambda_{\mathrm{laser}} = 532$ nm. When excited by the laser, the RhB particles emit fluorescence light at $\lambda_{\mathrm{RhB}} = 584$ nm. Both the RhB and MF particles also scatter the light from the illumination laser. The cloud of the particle mixture is observed by two cameras. One of the cameras is equipped with a (592 ± 43) nm bandpass filter blocking the scattered light from the illumination laser and most of the plasma glow. This camera (in the following denoted camera 2) captures only the RhB particles. The other camera (camera 1) is equipped with a (532 ± 10) nm bandpass filter to block the plasma glow and, hence, enhance the contrast. As it directly observes the scattered laser light, this camera captures all particles. In that way it is possible to distinguish between the particle species during the phase separation process.

The diameters of the used mixtures of MF and RhB particles, d_{MF} and d_{RhB}, respectively, can be found in Table I. The

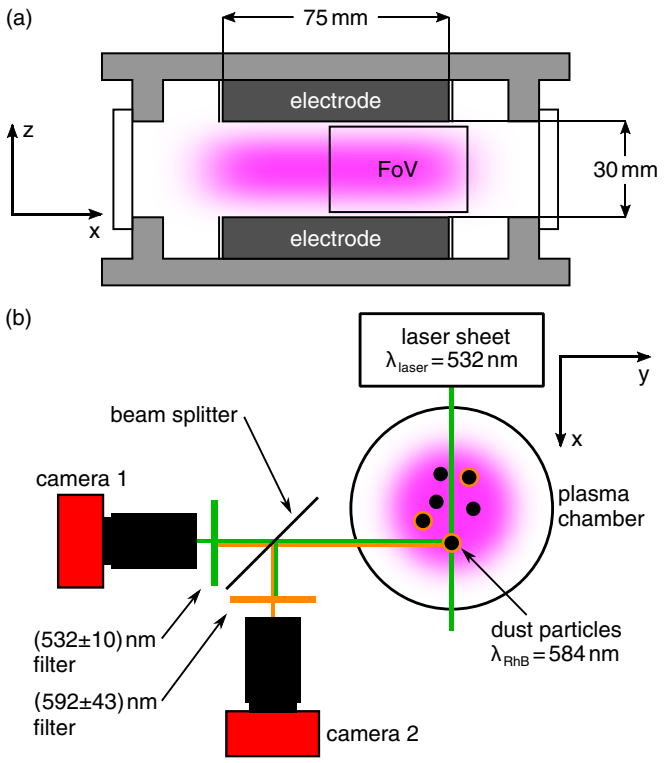

FIG. 1. (a) Side view and (b) top view of the experimental setup. The field of view of the cameras is denoted by FoV. The coordinate system introduced here will be used throughout the following analysis.

mean diameters and their standard deviation as given by the manufacturer are given here. Using the diameters of the MF and RhB particles, the relative size disparity can be written as

$$\varepsilon = \frac{\Delta d}{\bar{d}} = \frac{d_{\mathrm{RhB}} - d_{\mathrm{MF}}}{(d_{\mathrm{RhB}} + d_{\mathrm{MF}})/2}. \tag{2}$$

Defined in this way, $\varepsilon > 0$ when the RhB particles are larger than the MF particles and $\varepsilon < 0$ when they are smaller.

The two cameras observe the same area through a beam splitter. The field of view has a size of (45×30) mm^2 and covers slightly more than half of the (symmetric) dust cloud. Figure 1 shows a sketch of the geometry. The cameras have a spatial resolution of about 17 μm per pixel and can run at up to 385 fps (frames per second) at full resolution, enabling detection and tracking on the single-particle level. This gives us access to the particle fluxes $\vec{J}$ in the whole field of view. Combined with the possibility to distinguish between particle species, this makes a description of phase separation in binary dusty plasmas on the kinetic level possible.

The measurements presented here have been obtained during two parabolic flight campaigns in 2017 and 2018, consisting of four and three flight days, respectively. On each day 31 parabolas are flown, providing 22 s of microgravity per parabola. It is desirable to inject the needed amount of dust as quickly as possible at the beginning of each parabola, using multiple dust shakers filled with the same mixtures simultaneously. Because the number of dust shakers that can be mounted to the chamber is limited, at most four different particle mixtures can be used per flight day. On the 2017

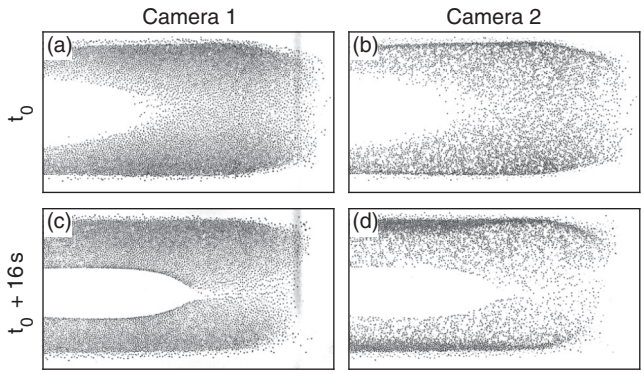

FIG. 2. The four panels show snapshots of both cameras at the start and at the end of a typical measurement. The images have been inverted and optimized to enhance the visibility of the particles. (a) and (c) Camera 1 (all particles); (b) and (d) camera 2 (fluorescent particles only). (a) and (b) Directly after stabilization of the dust cloud; (c) and (d) 16 s later.

campaign, mixtures no. 1 to no. 8, no. 13, and no. 14 (numbering according to Table I) were investigated, whereas on the 2018 campaign, mixtures no. 8 to no. 13, no. 15, and no. 16 were used. In total, 175 usable data sets could be obtained, all of which will later be used in Sec. IV.

III. THE DIFFUSION COEFFICIENT

In this section the data analysis is presented that makes use of the full phase-space information on the single-particle level to obtain (uphill) diffusion coefficients. The data quality allows us to obtain spatially resolved particle fluxes and densities of the two populations from which the diffusion coefficient can be calculated using Eq. (1).

A. Overview

First, to get an impression of the appearance of the data, (inverted) snapshots of one measurement are shown in Fig. 2. The same data set will also be used as an example throughout the following sections. The sequence was recorded at a frame rate of 200 fps. The pressure was 30 Pa, and the rf power 2 W. Dust combination no. 9 was used and, thus, the fluorescent particles were larger than the MF particles ($d_{\mathrm{MF}} < d_{\mathrm{RhB}}$, $\varepsilon = +0.04$). The four panels show the images of both cameras shortly after injection of the dust and stabilization of the dust cloud (top row) as well as 16 s later (bottom row). The phase separation can clearly be seen: At the beginning, the particles are distributed homogeneously across the whole dust cloud in both cameras, so the RhB and the MF particles are mixed. Later, camera 2 shows that the RhB particles agglomerate in the top and bottom parts of the cloud, exhibiting a much higher number density there than in the central region. This is the expected behavior according to the model of Killer *et al.* The ion drag force and the electric field force scale with d^2 and d, respectively. Hence, for the larger particles, the outward-pointing ion-drag force outbalances the inward-pointing electric field force, and the equilibrium position is shifted outwards compared to the smaller particles. Meanwhile, the overall dust distribution does not change significantly, as shown by camera 1. However, it can be seen that the total number of particles in the dust cloud decreases during the measurement, resulting in a decreasing overall particle number density. This is mainly caused by two dust-loss channels: First, particles leave the cloud at the outer edges due to imperfect confinement, and, second, there was a residual drift into the other (not observed) half of the chamber due to residual gravity, especially during the 2018 campaign.

After dust injection and stabilization of the cloud, the remaining measurement time of each parabola is about 10 to 15 s. To allow phase separation processes to take place during this time, ε must not be too small. On the other hand, when ε is chosen too large, the particle populations already separate during the insertion of the dust. As we are interested in the dynamics of the phase separation here, intermediate values of ε are chosen. As an estimation of relevant speeds, we consider a particle of the large species that travels from the void boundary to outer edge (distance about 10 mm) during the observation time (about 10 s), resulting in an observable phase separation speed of about 1 mm/s.

B. Particle tracking

We start the analysis of the phase separation sequence when most of the dust is visible in the region of interest and the void has started to form. The dust cloud does not have to be fully stabilized yet. The pull-out maneuver of the plane (when the apparent gravity changes from $0\,g$ to $1.8\,g$) marks the end of the analyzed sequence. Particles are detected in the entire sequence, and their positions are determined using the moment method [18,19] with an additional sobel filter. Typically, between 10 000 and 20 000 particles are found per frame. The particles are then tracked from frame to frame. The tracking algorithm is based on a Kalman filter for prediction and a nearest-neighbor search to find the best successor position of a particle in the current frame based on its previous positions. The velocity is determined by a central difference using three consecutive positions to obtain one velocity data point without further smoothing.

For a first overview of the particle dynamics, an overall flow field is calculated by averaging the particle velocities on a $2 \times 2\ \mathrm{mm}^2$ grid for the RhB particles. The result is shown in Fig. 3(a) as a temporal average over the entire sequence. The dust-loss channels to the top and bottom as well as to the left, out of the field of view, can clearly be seen. Furthermore, there is a double-vortex structure right of the void. Particles starting at the void flow to the right in the equatorial plane. They eventually separate into one upward-moving and one downward-moving stream that move to the left again close to the top and bottom edge of the cloud, respectively, and finally unite again near the void edge. The vortex is not completely closed, which hints at an out-of-plane motion that cannot directly be observed with our diagnostic. However, out-of-plane motion can be neglected for the analysis of the phase separation, which occurs in-plane. Figure 3(b) shows the curl of the velocity field $\vec{\nabla} \times \vec{v}$ revealing the vortex structure, indicated by the green and blue regions above and below the equatorial plane where the curl has an opposite sign but a similar absolute value.

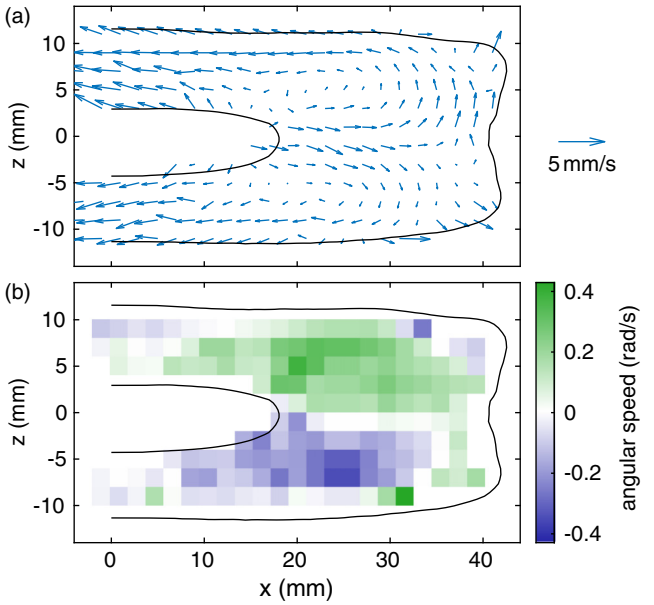

FIG. 3. Exemplary results of particle detection and tracking. The same data set as in Fig. 2 is shown, and the images of camera 2 (RhB particles) have been used. (a) Velocity field on a 2×2 mm^2 grid, temporally averaged over the whole data set. (b) Curl of the velocity field, calculated on the same grid as in (a) and averaged over the whole data set as well. The overlaid contour of the cloud was obtained from the particle density of camera 1.

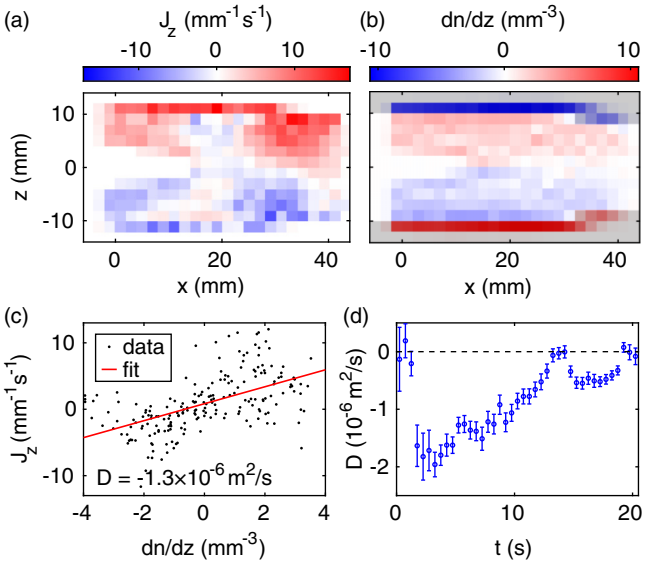

FIG. 4. Vertical component (a) of the flux J_z and (b) of the gradient of the particle number density. (c) Linear regression to obtain the diffusion coefficient. All data have been averaged over a 0.5 s interval in the middle of the measurement. (d) Diffusion coefficient from the linear regressions.

Such vortex structures have been investigated previously and are driven by the outward-pointing ion flow [20,21]. The typical flow speed of the particles due to the vortices is of the order of 1 mm/s and, hence, in the same range as the phase separation speed. Thus, the vortex motion and the phase separation are of comparable strength. While Fig. 3(a) clearly reveals the vortex motion, an outward motion, which would be expected for these RhB particles, is hardly seen. The vortex motion becomes suppressed at higher pressures ($p > 40$ Pa), but increasing the pressure is not a viable solution, because, then, insertion of the dust would be difficult and the formation of a stable cloud would take too long due to the higher neutral drag force at such high pressures. The phase separation would also be slowed even more and would not be observable in the available measurement time. Therefore, strategies have to be found to differentiate the phase separation from the vortex motion.

C. Diffusion flux and density

Basically, the diffusion coefficient is calculated from Eq. (1). As already mentioned and visible in Fig. 2, the larger species agglomerates mainly at the top and bottom of the dust cloud and not so much at the right of the field of view. It is therefore reasonable to consider only the z direction for the following calculation. With this, we have the relation

$$D = -\frac{J_z}{dn/dz}, \tag{3}$$

where J_z is the z component of the flux. With the velocity field from above we have the flux $\vec{J} = n\vec{v}$ on the grid. The particle number density n is obtained by counting detected particles on the same 2×2 mm^2 grid that has already been used before. Additionally, the density is calculated on a second grid that has the same mesh size, but is shifted by 1 mm in the z direction. This allows us to take the difference between two vertically adjoining grid cells to obtain the density gradient dn/dz at the positions of the main grid.

These calculations are done for each frame and then averaged over time slices of 0.5 s each. As we are interested in the dynamics of the phase separation, only positions from camera 2 are used. An instant from the middle of the sequence is shown in Figs. 4(a) and 4(b). It can be seen that when the RhB particles are the larger species, J_z is mostly positive above the equatorial plane and negative below it. This supports the observation that the RhB particles agglomerate at the top and bottom of the dust cloud. However, J_z shows traces of the vortex motion: Around $x = 20$ mm there are blue cells above and red cells below the equatorial plane, indicating a net flow towards the equatorial plane in these regions. Similarly, the outward-pointing flow at $x > 30$ mm (indicated by the intense red area above the equatorial plane and the blue area below it) is presumably higher than would be caused by the phase separation alone. It is therefore inappropriate to calculate a locally resolved diffusion coefficient from this flux as this would as well contain significant contributions by the vortex motion.

The density gradient has a nearly constant absolute value in the whole dust cloud with positive sign above and negative sign below the equatorial plane, meaning that the RhB density is constantly increasing with increasing distance from the equatorial plane. At the very top and bottom, distinct regions strike the eye where the gradient takes large values and an opposite sign compared to the rest of the respective

hemisphere of the dust cloud. These are simply caused by the sharp outer boundary of the dust cloud where the density drops from a large value to zero and are therefore not considered for further analysis. The corresponding grid cells are determined and excluded manually, as indicated by the shaded regions in Fig. 4(b).

D. Diffusion coefficient

Apart from the signatures of the vortex motion in the flux mentioned above, J_z and dn/dz are too noisy to calculate a locally resolved diffusion coefficient according to Eq. (3). Thus, the diffusion coefficient is determined by accounting for all grid points from the same time slice. The diffusion coefficient then results from a linear fit of the measured flux to the density gradient. In this way, the temporal resolution of 0.5 s can be preserved. An example of the fit is shown in Fig. 4(c) for the same time slice as in Figs. 4(a) and 4(b). Finally, the fits for all 0.5 s time slices yield the temporal evolution of the diffusion coefficient as shown in Fig. 4(d). The error of the diffusion coefficient was calculated from the error in the slope of the linear fit.

As already mentioned, the diffusion coefficient is negative because the particles exhibit uphill diffusion during the phase separation, further accumulating in areas where the density is already high. In the beginning, D is small during the dust injection and stabilization of the dust cloud and then quickly reaches a minimum at about $D = -1.5 \times 10^{-6}$ m^2/s between $t = 2$ s and $t = 8$ s. This is the main phase separation process. At $t > 8$ s the absolute value of D decreases again as more and more particles reach their equilibrium positions. Killer *et al.* [16] determined values of $D = -6.4 \times 10^{-6}$ m^2/s for the early stages and $D = -3.5 \times 10^{-7}$ m^2/s for the later stages of the separation process. Our value of $D = -1.5 \times 10^{-6}$ m^2/s lies well within this range, suggesting that the phase separation is as discussed in Ref. [16] driven by an imbalance of the ion drag and electric field forces on the particles.

As mentioned above, the analysis of the phase separation dynamics is possible only in a restricted range of ε. The size disparity where phase separation becomes observable during a parabola has been found to be about $|\varepsilon| \approx 0.03$. At smaller size disparities the phase separation is so slow that it cannot be detected within the measuring time provided by the parabolic flight or there is no phase separation at all. When the absolute value of the size disparity is larger than about $|\varepsilon| \approx 0.05$, both populations have already reached their equilibrium positions as the dust cloud settles, and there is no more motion that can be attributed to the phase separation. Therefore, the range of ε this method of determining D can be applied to is limited to about $0.03 < |\varepsilon| < 0.05$. We have also found that the method does not work for all data sets in this range, probably because the determination of $\vec{J}$ is very sensitive to disturbances due to vibrations and residual gravity. The temporal average of the diffusion coefficient $\bar{D}$ is collected in Table II for four data sets. Even though data sets have been selected for analysis that did not show obvious perturbations due to residual gravity, the diffusion coefficients for the two measurements using mixture no. 8 differ significantly.

TABLE II. Temporal average of the diffusion coefficient of four selected data sets. The mixture no. refers to the numbering in Table I. The relative size disparity is given here again.

Mixture no.	ε	$\bar{D}$ (10^{-6} m^2/s)
8	$+0.035 \pm 0.021$	-0.76
8	$+0.035 \pm 0.021$	-0.28
9	$+0.040 \pm 0.024$	-0.90
13	-0.053 ± 0.027	-0.58

IV. RADIAL POSITION AS A MEASURE FOR PHASE SEPARATION

Particle tracking is computationally expensive, hence it is not practicable to conduct the above analysis on a large number of data sets. On the other hand, a systematic study of the behavior of binary systems is desirable. In this section we will present a measure for the phase separation that relies on the particle positions only. As the particle detection itself takes only a small fraction of the computation time needed for the tracking as presented in Sec. III, the approach that follows is much faster.

Furthermore, while the possibility to follow the demixing process gives interesting insights, it limits methods that depend on it to small size disparities. The method that follows can also be applied to larger size disparities, when the phase separation already completes during the settling of the dust cloud.

The concept of the radial position

For each particle detected in a frame recorded at time t, a radial position parameter b is calculated according to the formula

$$b(i,t) = \frac{1}{12\text{mm}} \left\{ \left[\frac{x_i - \min(x_i, 12\text{ mm})}{4} \right]^2 + z_i^2 \right\}^{1/2}, \quad (4)$$

where (x_i, z_i) is the position of the ith particle detected in the respective frame. The distance $b_{\text{all}}(i,t)$ accounts for *all* particles seen in camera 1 and $b_{\text{RhB}}(i,t)$ for the fluorescent particles in camera 2. The calculation of the radial position has been chosen so that lines of constant distance follow the shape of the void and the dust cloud; see Fig. 5(a). Basically, it is a modification of the Euclidean distance between the particle and the $b = 0$ line where additionally the distance in the x

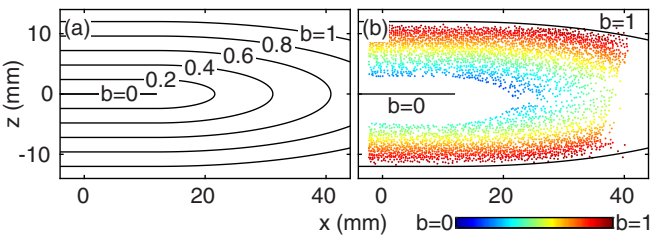

FIG. 5. (a) Definition of the radial position parameter b as given in the text. (b) Example for one frame from the beginning of the sequence. The detected particles of camera 2 are color-coded according to b. The solid lines denote $b = 0$ and $b = 1$, respectively.

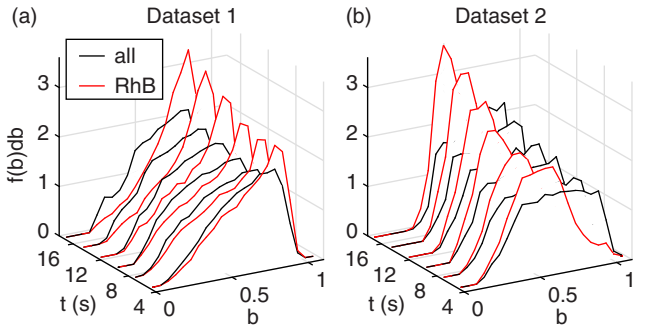

FIG. 6. Radial distribution of particles for (a) data set 1 and (b) data set 2. For each data set, six points in time are shown. The fluorescent particles ($f(b_{\mathrm{RhB}})$, red) accumulate at high b (data set 1) or low b (data set 2), respectively, whereas the overall distribution of particles ($f(b_{\mathrm{all}})$, black) nearly stays constant.

direction is scaled by a factor of 0.25. A value of zero means that a particle is in the center of the void. The scaling factor $1/12$ makes a particle at the outer edge of the cloud have a value of about one. Figure 5(b) shows the radial distance of the particles detected in one frame. It can be seen that the radial position defined above reflects the shape of a typical dust cloud quite well.

To demonstrate the further processing of the data, the example data set from the previous section ($d_{\mathrm{RhB}} > d_{\mathrm{MF}}$, $\varepsilon = +0.04$) is used again, denoted data set 1. Additionally, a second data set (data set 2) is added. That one uses dust combination no. 10 ($d_{\mathrm{RhB}} < d_{\mathrm{MF}}$, $\varepsilon = -0.09$), while all other parameters are the same as for data set 1. Due to the opposite sign of ε for the two data sets, opposite behavior is expected with regard to phase separation. The normalized histogram of all $b(i,t)$ belonging to the same frame t corresponds to the radial distribution of the particles. When camera 1 is used, we yield the overall radial dust distribution $f(b_{\mathrm{all}})db$, whereas when camera 2 is used, we yield the distribution of the RhB particles $f(b_{\mathrm{RhB}})db$. Figure 6 shows these distributions for both data sets. It can be seen that $f(b_{\mathrm{all}})db$ does not change much over time in both data sets. Note that there is no correction of the geometric effect that with increasing b a range of the same width corresponds to an increasing area. For data set 1, $f(b_{\mathrm{RhB}})db$ shows a peak at $b \approx 0.8$ right from the beginning that increases and steepens even more with time. This means that even before the dust cloud has fully stabilized, the larger RhB particles accumulate in the outer parts of the dust cloud as expected, and this effect continues. Data set 2 shows the inverse effect. Here a peak at $b \approx 0.4$ is present from the beginning and increases even more than in the case of data set 1. The more pronounced peak may be due to the larger absolute value of the size disparity compared to data set 1. In both examples, it can clearly be seen that the distributions of all and the fluorescent particles differ more and more as time progresses.

To get one step closer to the goal of having a single number to characterize the dust distribution, it is reasonable to take the mean over all particles

$$\bar{b}_{\mathrm{all}}(t) = \langle b_{\mathrm{all}}(i,t)\rangle_i,$$
$$\bar{b}_{\mathrm{RhB}}(t) = \langle b_{\mathrm{RhB}}(i,t)\rangle_i \qquad (5)$$

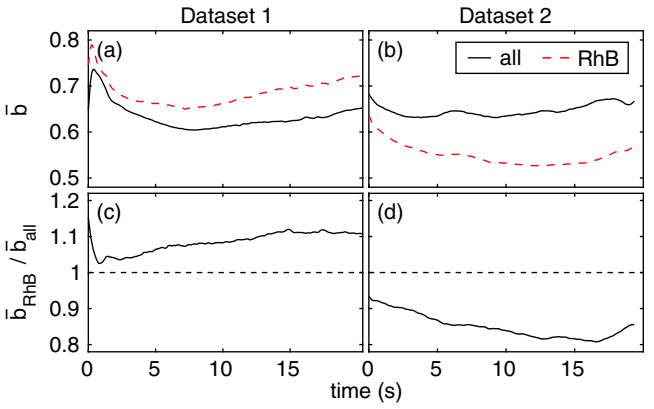

FIG. 7. Separation parameter averaged over all particles in each frame $\bar{b}_{\mathrm{all}}$ (all particles) and $\bar{b}_{\mathrm{RhB}}$ (fluorescent particles only) for (a) data set 1 and (b) data set 2 and (c) and (d) their respective ratio $\bar{b}_{\mathrm{RhB}}/\bar{b}_{\mathrm{all}}$.

for each frame and each camera. The result can be seen in Figs. 7(a) and 7(b). As expected, $\bar{b}_{\mathrm{RhB}}$ is larger than $\bar{b}_{\mathrm{all}}$, and the difference is constantly increasing in the case of data set 1, where the fluorescent particles are the larger species and accumulate on the outer edge of the cloud. For data set 2, where the fluorescent particles are the smaller species and accumulate close to the void edge, $\bar{b}_{\mathrm{all}}$ is increasingly smaller than $\bar{b}_{\mathrm{RhB}}$. There are fluctuations on the timescale of several seconds that affect $\bar{b}_{\mathrm{all}}$ and $\bar{b}_{\mathrm{RhB}}$ in the same way. For example, an overall shift of the dust cloud due to residual gravity, especially in the x direction, can cause such a behavior. To proceed further, the ratio $\bar{b}_{\mathrm{RhB}}/\bar{b}_{\mathrm{all}}$ is used as it reflects the differences between the two populations in a single number per frame while it compensates for common, unwanted fluctuations. Figures 7(c) and 7(d) show this ratio for both data sets. Values of $\bar{b}_{\mathrm{RhB}}/\bar{b}_{\mathrm{all}} > 1$ mean that the RhB particles accumulate outside of the MF population, and $\bar{b}_{\mathrm{RhB}}/\bar{b}_{\mathrm{all}} < 1$ means that the RhB particles are closer to the void than the MF population.

V. RESULTS AND DISCUSSION

Averaging the ratio $\bar{b}_{\mathrm{RhB}}/\bar{b}_{\mathrm{all}}$ again, this time over all frames of a sequence, yields the temporally averaged mean distance ratio

$$B = \langle \bar{b}_{\mathrm{RhB}}(t)/\bar{b}_{\mathrm{all}}(t)\rangle_t \qquad (6)$$

as a single parameter quantifying this data set. The presented analysis has been done for all 16 mixtures from Table I, and the results are shown in Fig. 8. For each of the mixtures, between three and 21 usable data sets could be obtained, yielding a total of 175 data sets shown individually in Fig. 8(a). We have verified that the data points from the same mixture but different flight days and even campaigns overlap. Hence, there seems to be no systematic error due to the dispenser positioning or other external conditions that might vary on long timescales. The dust mixtures can be divided into two groups: one with sizes of about 4 μm (no. 1 to no. 6 according to Table I) and one with sizes of about 7 μm (no. 7 to no. 16). It can be seen that the data points for the two groups

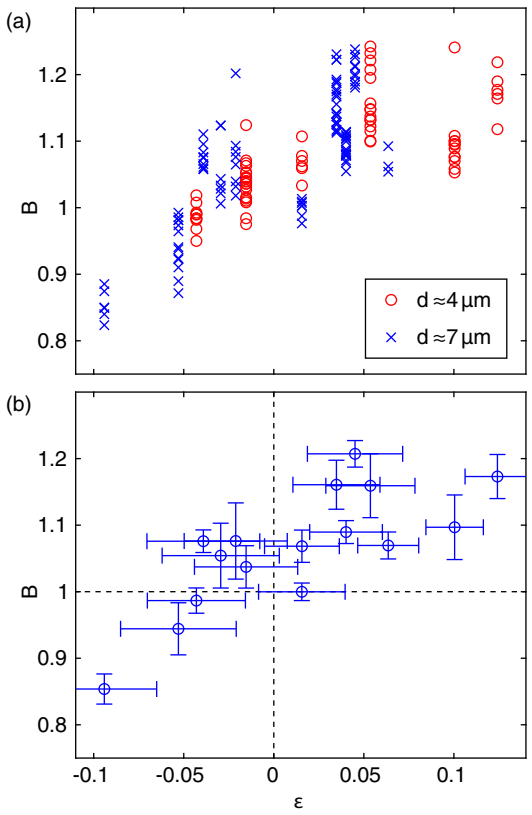

FIG. 8. Space- and time-averaged separation parameter of all analyzed data sets. (a) Individual data points. Red circles show mixtures with a mean diameter in the 4 μm range, whereas blue crosses show data sets with a mean diameter in the 7 μm range. (b) Mean values and standard deviations of ε and B for each mixture. There is a clear correlation between the two quantities. The dashed lines indicate the expected center of symmetry.

basically lie on the same curve; When considering points of similar ε, the scatter of the points from either the small or the large dust is comparable to the scatter of points from both groups. Consequently, there is no influence of the absolute particle size on the phase separation. Regarding the particle sizes, the relative size disparity seems the only quantity that determines the phase separation. Furthermore, we did not find any significant influence of the neutral gas pressure, rf power, or the amount of dust on the phase separation.

It should be mentioned here that the selection of particle diameters is limited to the batches available from the manufacturer. Therefore, the dust sizes cannot be chosen completely freely, and there are no two mixtures with the exact same ε. Instead, all data points sharing the same size disparity were obtained using the same mixture. Since we have more than one measurement for each mixture, it is possible to determine the mean and the standard deviation of B for each mixture, which are shown in Fig. 8(b). The error bars for ε have been taken from Table I. Note that these give the width of the distribution of particle diameters and not the uncertainty of the mean.

There is a clear trend towards increasing B with increasing size disparity. This is expected when considering the model by Killer *et al.* [16], where the difference of the plasma forces increases with increasing size disparity. However, the relation between ε and B is not completely linear. Instead, there seems to be a saturation at $B \approx 1.15$ for $\varepsilon > 0.04$. Neglecting this saturation for the moment and considering only the nearly linear part ($\varepsilon \leqslant +0.04$), one would expect a symmetric behavior around the point ($\varepsilon = 0, B = 1$) due to the fact that equally sized particles that do not separate at all yield $B = 1$. But interestingly, there seems to be a shift towards higher B, and the data points are symmetric around ($\varepsilon = 0, B \approx 1.1$). Practically, this means that the RhB particles tend to accumulate at the outer parts of the cloud more than one would expect considering only the particle sizes. To make the particles accumulate near the void ($B < 1$), we had to use mixtures with $\varepsilon < -0.05$, whereas for $-0.04 < \varepsilon < 0$, we have $B > 1$.

This leads us to the conclusion that there is a systematic additional effect between the different dust species. There might be differences between the plasma forces neglected here. In our case, there could be influences during the storage of the particles, e.g., the particles might aggregate water from the air over time. Because not all particles for one experiment have been purchased at the same time, there is a possibility that the MF and the RhB particles of a mixture have undergone different aging processes. This would explain differences between mixtures with similar ε. For example, the mixtures around $\varepsilon \approx +0.05$ show a large variation in B. An aging effect that affects one of the particle types more than the other would explain the overall shift towards higher B. Aging could modify the surface properties of the particles as well as their density and size. Regarding the particle size, the diameter given by the manufacturer may not be accurate enough anymore at the point the particles are finally used in our experiments. Discrepancies between the provided size and microscopic as well as Mie ellipsometry measurements have already been found earlier [22–24]. Although *in situ* diagnostics of the dust size have recently been performed with high precision [25], it was not possible to implement a similar diagnostic in our experiment due to technical restrictions. A change of the particle mass or size during the measurement can be caused by outgassing of water [24,26], etching in the plasma [22,25,27,28], or the deposition of sputtered material [26]. Those effects are unlikely in our case because the particles are used for only about 20 s and discarded after each parabola. Furthermore, MF particles in a low-power argon discharge are not susceptible to etching.

Up to here, it has been assumed that the OML charging model applies and the particle charge is proportional to the particle size with the same proportionality factor for both particle species. However, if the electron and ion currents onto the particles were influenced by their surface properties, MF and RhB particles of the same size could attain different charges. Likewise, modified ion trajectories would lead to different ion drag forces on the two species. It is generally believed that charging mechanisms other than charge collection are negligible in laboratory dusty plasma experiments like ours. However, if phenomena such as secondary emission, photoemission, or thermal emission, which depend on the surface properties, played only a minor role, the resulting effect on the charge could suffice to explain the observed behavior. This question has to be set aside for further high-

precision measurements which might give interesting insights into the basic principles of dusty plasma physics.

Additional laser forces might play a role here. When laser photons are absorbed by the RhB particles and fluorescence photons are emitted isotropically, the resulting momentum transfer is different than for scattering, and this could influence the phase separation. However, as the laser penetrates the observation volume from the side, the additional force is expected to point sidewards, whereas we analyze the motion in the vertical direction.

The saturation at $B \approx 1.15$ that was mentioned earlier may be caused by our method: In the cases where B reaches values of about 1.2, the particles already separate during dust injection and stabilization of the dust cloud and are already completely separated at the beginning of the analyzed sequence. Using our method, we cannot track even faster separation because there is no possibility to determine (or even sensibly define) the radial position of a particle in a cloud that is still forming and rapidly changing its shape. But, in contrast to the method from Sec. III, which depends on tracking the process, it is still possible to yield a meaningful B when the analysis is started after the phase separation has already completed.

As can be seen in Fig. 8(b) it would be interesting to perform the experiment with particles with a narrower size distribution. Our method handles overlapping size distributions of the RhB and the MF particles correctly. Spatial regions that contain particles of both species appear in both distributions $f(b)db$ and, hence, are accounted for in the same way in the determination of B. But narrower size distributions would result in more well-defined data points. Furthermore, an *in situ* size diagnostic would allow an analysis independent of potential aging of the particles.

VI. SUMMARY

In a dusty plasma experiment under microgravity, phase separation has been found even for small size disparities far below the threshold for spinodal decomposition. We have used high-resolution video cameras that allowed us to follow the phase separation process on the kinetic level. Spatially resolved particle fluxes and densities were determined. From those quantities, diffusion coefficients could be extracted that describe the phase separation. We obtained values of about $D = -1.5 \times 10^{-6}\ \mathrm{m}^2/\mathrm{s}$, which is negative because the particles exhibit uphill diffusion. The order of magnitude suggests that the phase separation is driven by an imbalance in ion drag and electric field forces.

Furthermore, a method has been presented that allows to quickly characterize measurements with respect to their phase-separation behavior. A total of 175 data sets have been analyzed that span relative size disparities from about $\varepsilon = -0.1$ to $\varepsilon = +0.125$ using 16 different particle mixtures. It has been found that the results are reproducible among different flight days and even campaigns. A linear dependence between the size disparity and the strength of the phase separation has been found. The phase separation depends only on the size disparity of the particles and not on the absolute particle size.

ACKNOWLEDGMENTS

Financial support by Deutsches Zentrum für Luft- und Raumfahrt (DLR) under Contracts No. 50WM1638 and No. 50WM1962 is gratefully acknowledged. The authors would like to thank Peter Druckrey for technical support.

[1] J. S. Huang, W. I. Goldburg, and A. W. Bjerkaas, Phys. Rev. Lett. **32**, 921 (1974).
[2] D. Beysens, P. Guenoun, and F. Perrot, Phys. Rev. A **38**, 4173 (1988).
[3] M. Carpineti and M. Giglio, Phys. Rev. Lett. **68**, 3327 (1992).
[4] A. E. Bailey, W. C. K. Poon, R. J. Christianson, A. B. Schofield, U. Gasser, V. Prasad, S. Manley, P. N. Segre, L. Cipelletti, W. V. Meyer *et al.*, Phys. Rev. Lett. **99**, 205701 (2007).
[5] K. Yoshizawa, N. Wakabayashi, M. Yonese, J. Yamanaka, and C. P. Royall, Soft Matter **8**, 11732 (2012).
[6] S. Katano and M. Iizumi, Phys. Rev. Lett. **52**, 835 (1984).
[7] B. D. Gaulin, S. Spooner, and Y. Morii, Phys. Rev. Lett. **59**, 668 (1987).
[8] P. Wiltzius, F. S. Bates, and W. R. Heffner, Phys. Rev. Lett. **60**, 1538 (1988).
[9] M. Mikikian, L. Boufendi, A. Bouchoule, H. M. Thomas, G. E. Morfill, A. P. Nefedov, V. E. Fortov, and the PKE-Nefedov team, New J. Phys. **5**, 19 (2003).
[10] G. E. Morfill, U. Konopka, M. Kretschmer, M. Rubin-Zuzic, H. M. Thomas, S. K. Zhdanov, and V. Tsytovich, New J. Phys. **8**, 7 (2006).
[11] K. R. Sütterlin, A. Wysocki, A. V. Ivlev, C. Räth, H. M. Thomas, M. Rubin-Zuzic, W. J. Goedheer, V. E. Fortov, A. M. Lipaev, V. I. Molotkov *et al.*, Phys. Rev. Lett. **102**, 085003 (2009).
[12] J. W. Cahn, J. Chem. Phys. **42**, 93 (1965).
[13] K. R. Sütterlin, H. M. Thomas, A. V. Ivlev, G. E. Morfill, A. M. Fortov, V. E. Lipaev, V. I. Molotkov, O. F. Petrov, A. Wysocki, and H. Löwen, IEEE Trans. Plasma Sci. **38**, 861 (2010).
[14] C.-R. Du, K. R. Sütterlin, K. Jiang, C. Räth, A. V. Ivlev, S. Khrapak, M. Schwabe, H. M. Thomas, V. E. Fortov, A. M. Lipaev *et al.*, New J. Phys. **14**, 073058 (2012).
[15] A. V. Ivlev, S. K. Zhdanov, H. M. Thomas, and G. E. Morfill, EPL (Europhys. Lett.) **85**, 45001 (2009).
[16] C. Killer, T. Bockwoldt, S. Schütt, M. Himpel, A. Melzer, and A. Piel, Phys. Rev. Lett. **116**, 115002 (2016).
[17] M. Klindworth, O. Arp, and A. Piel, J. Phys. D **39**, 1095 (2006).
[18] J. C. Crocker and D. G. Grier, J. Colloid Interface Sci. **179**, 298 (1996).
[19] Y. Ivanov and A. Melzer, Rev. Sci. Instrum. **78**, 033506 (2007).
[20] M. Schwabe, S. Zhdanov, C. Räth, D. B. Graves, H. M. Thomas, and G. E. Morfill, Phys. Rev. Lett. **112**, 115002 (2014).

[21] T. Bockwoldt, O. Arp, K. O. Menzel, and A. Piel, Phys. Plasmas **21**, 103703 (2014).
[22] G. H. P. M. Swinkels, E. Stoffels, W. W. Stoffels, N. Simons, G. M. W. Kroesen, and F. J. de Hoog, Pure Appl. Chem. **70**, 1151 (1998).
[23] B. Liu, J. Goree, V. Nosenko, and L. Boufendi, Phys. Plasmas **10**, 9 (2003).
[24] C. Killer, M. Mulsow, and A. Melzer, Plasma Sources Sci. Technol. **24**, 025029 (2015).
[25] O. H. Asnaz, H. Jung, F. Greiner, and A. Piel, Phys. Plasmas **24**, 083701 (2017).
[26] J. Carstensen, H. Jung, F. Greiner, and A. Piel, Phys. Plasmas **18**, 033701 (2011).
[27] W. W. Stoffels, E. Stoffels, G. H. P. M. Swinkels, M. Boufnichel, and G. M. W. Kroesen, Phys. Rev. E **59**, 2302 (1999).
[28] H. Jung, F. Greiner, O. H. Asnaz, J. Carstensen, and A. Piel, Phys. Plasmas **22**, 053702 (2015).